Macromolecules

pubs.acs.org/Macromolecules Article

Structural Evolution of Ternary Amphiphilic Block Copolymer Solvent Systems for Phase Inversion Membrane Formation

Yusuke Hibi, Sarah A. Hesse, Fei Yu, R. Paxton Thedford, and Ulrich Wiesner*

Cite This: *Macromolecules* 2020, 53, 4889−4900

Read Online

ACCESS | Metrics & More | Article Recommendations | Supporting Information

Downloaded via CORNELL UNIV on June 23, 2020 at 15:39:13 (UTC).
See https://pubs.acs.org/sharingguidelines for options on how to legitimately share published articles.

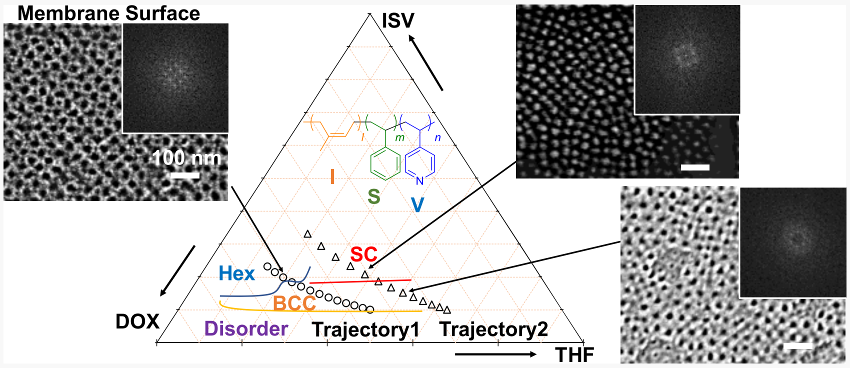

ABSTRACT: Block copolymer (BCP)-derived asymmetric ultrafiltration membranes combine the BCP self-assembly with nonsolvent-induced phase separation (SNIPS). To understand the structural evolution in membrane top separation layers made from polyisoprene-*b*-polystyrene-*b*-poly(4-vinylpyridine) (ISV) in dioxane (DOX) and tetrahydrofuran (THF) all the way to the final membrane, we combined solution small-angle X-ray scattering (SAXS), estimated solution concentrations and compositions upon solvent evaporation, *in situ* grazing-incidence SAXS (GISAXS), spin−spin relaxation time (T_2) analysis by solution ^{1}H NMR, and scanning electron microscopy (SEM). Above the critical micelle concentration (<1 wt % ISV), solvent evaporation drives micelles with poly(4-vinylpyridine) (P4VP) in the core across disorder-to-order and order-to-order transitions, the latter in part driven by the segregation of polyisoprene (PI)- from polystyrene (PS)-blocks. Extended to polystyrene-*b*-poly(4-vinylpyridine) (SV) in dimethylformamide (DMF) and THF, results suggest that, in particular, T_2 relaxation analysis by ^{1}H NMR is a powerful tool in analyzing which blocks form micelle core and which form corona chains. We expect insights to help develop next-generation SNIPS membranes for applications, *e.g.*, in clean water and biopharmaceutical separations.

■ INTRODUCTION

Periodic mesoscale structures arising from the self-assembly (SA) of block copolymers (BCPs) have been widely studied in both the solution state and the bulk.[1,2] Even in solution, where structural relaxation times are faster than in the bulk, structural transitions away from equilibrium are commonly observed.[3,4] Timely quenching of such transiting structures could enable access to structures different from those expected from equilibrium conditions.[5−7] One successful application of such a nonequilibrium approach to the BCP structure formation is in BCP-derived asymmetric ultrafiltration membranes obtained from the combination of BCP SA with nonsolvent-induced phase separation (NIPS), the so-called SNIPS-derived membranes.[8−10] This new class of membranes consists of a surface layer of periodically ordered mesopores atop a disordered (DO) asymmetric substructure with graded meso- to macropores. The high pore density and narrow pore size distribution of the top separation layer provide SNIPS membranes with a combination, respectively, of high flux and high resolution in separation applications not achievable with conventional NIPS-derived membranes.[11]

The SNIPS process is initiated by casting or doctor-blading a thin film of BCP solution. Most frequently, the BCP solutions are prepared in the semidiluted regime (10−20 wt %) with binary solvents. Immediately after casting, the solution composition begins to change due to solvent evaporation, *i.e.*, the BCP concentration and volume fraction of the less volatile solvent increase. This change in composition may cause BCP phase transitions in solution.[12,13] After the brief evaporation period, usually in the range of 10−120 s, the transiting structure is quickly quenched by immersion into a nonsolvent

Received: March 15, 2020
Revised: April 28, 2020
Published: June 3, 2020

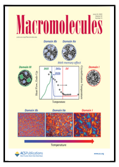

ACS Publications © 2020 American Chemical Society

https://dx.doi.org/10.1021/acs.macromol.0c00595
Macromolecules 2020, 53, 4889−4900

deionized water bath, precipitating the solidified final membrane structure. In this context, the investigation of the BCP SA in solution is thus particularly crucial for the understanding of the membrane structure. BCP SA first occurs in the top surface separation layer and is responsible for the formation of dense, periodically ordered pores found in the final membrane, which determine the performance in separation applications.

BCPs well studied for this purpose are the diblock copolymer polystyrene-*b*-poly(4-vinylpyridine) (SV)[8,14−19] and the triblock terpolymer polyisoprene-*b*-polystyrene-*b*-poly(4-vinylpyridine) (ISV).[9,10,13,20−22] By exploiting solution small-angle X-ray scattering (SAXS) and *in situ* grazing-incidence SAXS (GISAXS) techniques, it has been elucidated that micellar packing, in a hexagonal (Hex) lattice for SV and in body-centered cubic (BCC) or simple cubic (SC) lattices for ISV, is key to obtaining the highly ordered surfaces in the final membranes.[9,13,20] As reported before, however, there is an apparent inconsistency between solution SAXS and *in situ* GISAXS results for ISV in particular.[13] Solution SAXS of ISV in 7:3 1,4-dioxane (DOX)/tetrahydrofuran (THF) (ISV/DOX/THF) exhibited scattering consistent with the BCC lattices and inconsistent with the SC lattices over a wide range of concentrations (10−20 wt %), whereas *in situ* GISAXS of an identical ISV/DOX/THF solution cast at 10 wt % instead suggested the presence of SC lattices. This inconsistency may arise from the difference between the steady/equilibrium-state solution SAXS and *in situ* GISAXS experiments, the latter collecting scattering patterns under continuous solvent evaporation-induced compositional changes after doctor blading.[9,13] Furthermore, particular ISVs of a relatively small molar mass (43 kDa) as compared to more frequently used medium molar mass ISVs (90−120 kDa) showed a phase transition from BCC to SC when monitored by *in situ* GISAXS.[13]

Questions arising from these earlier results clearly demonstrate the need for a more comprehensive study of the structural evolution of such ternary systems (BCP and two distinct solvents) in solution. The first attempt to this end was conducted for the system of polystyrene-*b*-poly(2-vinylpyridine) (PS-*b*-P2VP or S2V) in *N*,*N*-dimethylformamide (DMF) and THF (S2V/DMF/THF).[12] This work demonstrated that structural evolution is driven by solvent composition changes, which directly affect the effective volume fractions of PS and P2VP blocks; PS and P2VP are selectively swollen by THF and DMF, respectively. In contrast, in a binary solvent system consisting of two similar solvents like DOX and THF, as employed in the ISV system-based SNIPS process, the effective volume fraction changes of the constituent polymer blocks upon solvent compositional variations should be much smaller as compared to that of the S2V/DMF/THF system, which complicates the analysis. Another issue is that although the importance of micellar packing for SNIPS membrane formation is widely accepted, in particular for the top surface separation layer, the question about micellar structure itself, *i.e.*, which are the core- or corona-forming blocks, has remained under debate. This remains the case even after extensive studies based on considerations of solubility parameters,[19] small-angle neutron scattering (SANS) experiments,[17] as well as cryo-electron microscopy (cryo-EM),[19] atomic force microscopy (AFM),[14] and dynamic light scattering investigations.[15] A more comprehensive understanding of the micellar structure as a function of solvent composition will be crucial in the design of more advanced SNIPS membranes, *e.g.*, for the control of the spatial distribution of constituent BCPs in blended membranes based on the immiscibility between different species of micelles, micelle−solvent interactions, and surface energies of micelles.[23]

Herein, we propose such a comprehensive analysis of the solvent composition-driven structural evolution of the ISV/DOX/THF system by converging results from solution SAXS, *in situ* GISAXS, the study of polymer chain dynamics based on spin−spin relaxation time (T_2) analysis using solution ^{1}H NMR spectroscopy, and scanning electron microscopy (SEM) observations of the final membrane top surface. First, we will develop a ternary phase diagram for ISV/DOX/THF based on solution SAXS. Various ordered phases, including hexagonal cylinders, BCC-packed micelles, and SC-packed micelles, will be described over a wide range of DOX/THF ratios (from 9:1 to ∼4:6) for BCP concentrations beyond a disorder-to-order transition around 10 wt % ISV. These structures in solution as revealed by X-ray scattering will then be correlated with observations of membrane top surface structure after SNIPS as evidenced by SEM. Finally, we will describe polymer dynamics studies based on solution NMR, which will show how the polymer structure evolves from single chains to self-assembled structures (single chain → disordered micelles → BCC micelles → SC micelles) with solvent composition and increasing concentration. As these NMR studies can determine the core- and corona-forming blocks in such ternary solvent systems, the same NMR analysis of polymer chain dynamics will finally be extended to the SV/DMF/THF system, to provide a comparison with another well-studied system for the generation of SNIPS membranes.

EXPERIMENTAL SECTION

Block Copolymers. ISV and SV block copolymers were synthesized by sequential living anionic polymerization as reported before.[8,21] The total molar masses were 90 kDa (ISV) and 95 kDa (SV). ISV block volume fractions were 22:51:27 (polyisoprene (PI)/PS/poly(4-vinylpyridine) (P4VP)) and SV block volume fractions were 80:20 (PS/P4VP). Densities used to convert mass fractions into volume fractions were 0.91 g/cm^3 for PI, 1.0 g/cm^3 for PS, and 1.2 g/cm^3 for P4VP. Polymer dispersities were 1.12 for ISV and 1.13 for SV. Please note that we used ISV with a slightly larger P4VP-block fraction, mostly at the expense of the PI-block fraction as compared to earlier ("regular") ISV compositions around 30:55:15.[13,21,24] This ISV composition resulted in more well-defined solution SAXS patterns as compared to regular ISV, which facilitated the lattice assignments of micellar structures.

Solution SAXS. ISV BCP powder was dissolved in DOX/THF binary solvents at various solvent weight ratios and polymer concentrations, the latter ranging from 10 to 20 wt %, as discussed in the text. Solutions were sealed in 0.9 mm diameter capillaries (Charles Supper Co.) and subjected to SAXS experiments at the G1 beamline of the Cornell High Energy Synchrotron Source (CHESS). The X-ray wavelength used was 0.11 nm with a sample-to-detector distance of 2 m, and the exposure time was 1 s. Two-dimensional (2D) scattering patterns were recorded on an EIGER 1M pixel detector and converted to one-dimensional (1D) intensity profiles by integration along the radial direction processed *via* the Nika and Irena package for IGOR Pro7.[25,26]

Membrane Fabrication and SEM Characterization. A typical membrane fabrication process involved the following protocol: 30 mg ISV powder was dissolved in 270 mg of 5:5 or 3:7 DOX/THF (by weight) by overnight stirring at room temperature. The homogeneous solution was cast on a glass substrate and left for a specifically timed period of solvent evaporation, as detailed in the main text. The membrane was then immersed into an iced water bath (around 4 °C).

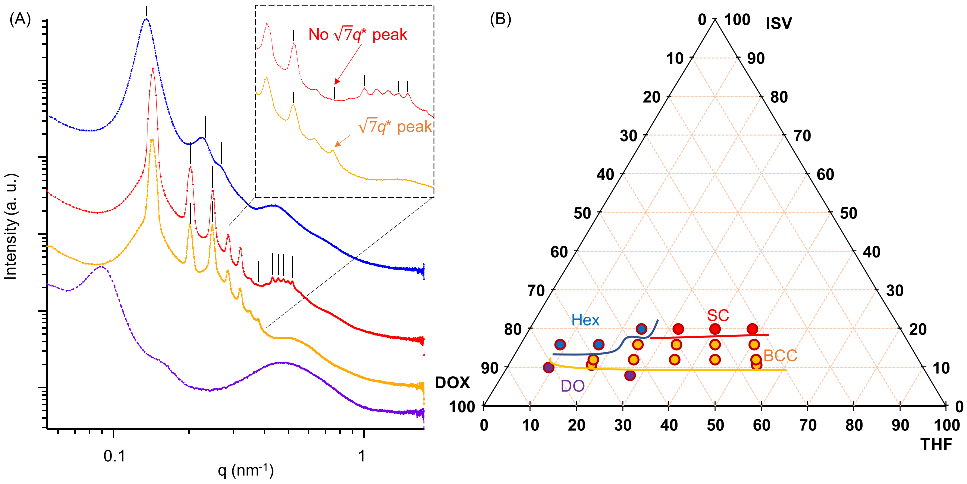

Figure 1. Ternary phase diagram of ISV/DOX/THF elucidated by solution SAXS experiments. (A) Representative SAXS profiles (from top to bottom) of (blue) hexagonal cylinders for 20 wt % ISV in 7:3 DOX/THF, (red) SC lattice for 20 wt % ISV in 4:6 DOX/THF, (yellow) BCC lattice for 16 wt % ISV in 4:6 DOX/THF, and (purple) disordered (DO) micelles for 10 wt % ISV in 9:1 DOX/THF. BCC and SC lattices were distinguished by the existence or nonexistence of a peak at $q = \sqrt{7}q^*$ for BCC and SC, respectively (see the inset). Note that all BCC and SC SAXS patterns gave more than seven peaks (see Figure S1 for a collection of all measured SAXS profiles). (B) ISV/DOX/THF ternary phase diagram based on the analysis of all SAXS experiments.

The entire process was conducted in a home-built plastic box, where the humidity was controlled in the range of 35−45% (relative humidity) either by increasing the humidity using a water bath or decreasing the humidity using nitrogen purging. The casting temperature aligned with the room temperature around 18 °C. After leaving the membrane in water overnight, the membrane was dried under ambient conditions, and the surface structure was characterized using a Zeiss Gemini 500 SEM with the secondary electron in-lens probe with a 1 kV acceleration voltage and an Everhart−Thornley detector. Membranes were Au−Pd-sputtered using a Denton Desk V instrument for 15 s with 20 mA current prior to SEM observations.

***In Situ* GISAXS.** The sample for GISAXS was prepared by dissolving ISV in 5:5 DOX/THF at 10 wt %. This solution was cast at the GISAXS D1 beamline stage at CHESS using a custom-built doctor-blading setup. The doctor blade was set at a 200 μm gate height. After blading, the sample was intermittently irradiated with X-rays for 1 s, with 3 s intervals at an incident angle of 0.15° and 2D scattering patterns collected on a PILATUS 200k detector, all under continuous solvent evaporation and under ambient environmental conditions (22 °C and 32% relative humidity), which were not controlled. The X-ray wavelength used was 0.12 nm with a sample−detector distance of 1.8 m. The 2D scattering patterns recorded on the PILATUS 200k detector were indexed with indexGIXS.[27−29]

^{1}H NMR Experiments. NMR samples were prepared in the following way. The ISV or SV BCP powders were dissolved in DOX-d_8/THF-d_8 or DMF-d_7/THF-d_8, respectively, at solvent ratios as discussed in the main text and at concentrations in the range of 0.1−20 wt %. The solutions were stirred for at least 1 day to ensure homogeneity. The solutions were then transferred into NMR tubes and degassed by sonication for several minutes. Nitrogen gas was then introduced into the NMR tubes to purge out oxygen. The tubes were then quickly sealed with lids. NMR experiments were conducted on an INOVA 600 spectrometer with an H{C/N} *XYZ*-PFG probe. For spin−spin relaxation time (T_2) experiments, the following Carr−Purcell−Meiboom−Gill (CPMG) sequence was used: [−relaxation delay−90° x pulse−(t_d−180° y pulse−t_d)$_n$−acquisition], where t_d is the pulse interval and n is the cycle number.[30] The transverse magnetization induced by the first 90° x pulse was dephased during a decay time of $2nt_d$, before acquiring the free induction decay (FID) signal. The decay time was logarithmically increased from 4 ms to 1.5 s with 15 steps. The signal intensity exponentially decreased as a function of increasing decay time, which provided the desired relaxation time T_2. The relaxation delay was set to 5 times the spin−lattice relaxation time (T_1). For T_2 analysis of polymers, the relaxation delay was set to 15 s as the longest T_1 of polymeric protons was around 2.7 s. For T_2 analysis of solvent molecules, the decay time was increased from 10 ms to 60 s and the relaxation delay was set to 90 s due to much slower T_2 and T_1 relaxations as compared to that of polymers. As detailed in the Results and Discussion section, the pulse interval in the echo train of the CPMG sequence was the crucial parameter, in particular for the SV/DMF/THF system. Most experiments were conducted with a 1 ms pulse interval, unless otherwise specified. For very quick relaxations of P4VP in THF/DOX (<10 ms), single pulse proton NMR spectra were used for plotting signal intensities at a decay time of 0 s. The T_2 relaxation as a function of decay time was fitted by single- or biexponential decays with IGOR Pro7, as described in the Results and Discussion section.

■ RESULTS AND DISCUSSION

Scattering Investigations of Ternary System ISV/DOX/THF. To generate an ISV/DOX/THF ternary phase diagram around the region relevant for the SNIPS membrane formation, a number of solutions in the concentration range of 8−20 wt % with various DOX/THF ratios (9:1−4:6) were subjected to SAXS experiments. Representative SAXS profiles are shown in Figure 1A. A comprehensive collection of scattering profiles is presented in Figure S1, and analysis results are summarized in Table S1 in the Supporting Information. Scattering patterns of solutions were consistent with one of the following four structures: hexagonal (Hex) cylinders, micelles packed in a simple cubic (SC) lattice, micelles packed in a body-centered cubic (BCC) lattice, or disordered (DO) micelle. All BCC and SC profiles exhibited seven or more peaks, which enabled us to distinguish BCC from SC lattices; compared to patterns exhibiting BCC lattices, scattering patterns resulting from an SC lattice lacked the peak at a scattering vector $q = \sqrt{7}q^*$, where q^* is the scattering vector of the primary peak (see the inset in Figure 1A). From these results, the ISV/DOX/THF ternary phase diagram shown in Figure 1B was derived. At low polymer concentrations of less than 10 wt %, scattering patterns showed only broad features with no discernible underlying lattices. As we will discuss below, NMR studies revealed that ISV forms micelles (with V

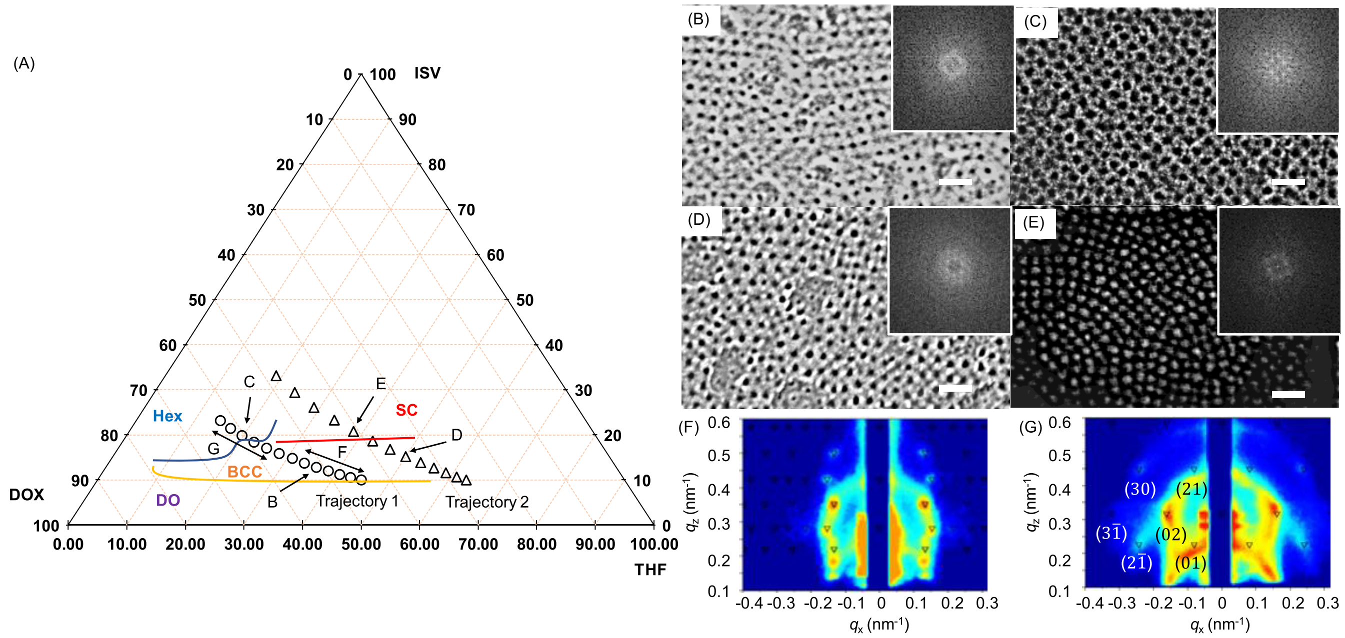

Figure 2. Structural evolution of the ISV/DOX/THF system during solvent evaporation. (A) Predicted compositional changes caused by evaporation are depicted in the experimental ISV/DOX/THF phase diagram from Figure 1 in 10 s intervals. Trajectory 1 (circles) starts from 5:5 DOX/THF, while trajectory 2 (triangles) starts from 3:7 DOX/THF, for 10 wt % polymer solution concentrations. SEM images of membrane top surfaces cast from 10 wt % ISV solutions in 5:5 DOX/THF with evaporation times of (B) 40 s and (C) 100 s, and in 3:7 DOX/THF with evaporation times of (D) 50 s and (E) 80 s. The quenching points are indexed along trajectories 1 and 2 in (A). The insets in (B)−(E) show fast Fourier transformations (FFTs) from parts of the SEM images (256 × 256 pixels) after binarization. The scale bars are all 100 nm. (F, G) *In situ* GISAXS patterns for trajectory 1. A 10 wt % ISV solution in 5:5 DOX/THF was cast, and then the structural evolution caused by evaporation was monitored by in situ GISAXS. At an evaporation time of 40 s (F), the GISAXS pattern is consistent with a BCC lattice with the ⟨110⟩ direction parallel to the membrane film normal direction and a lattice constant of 58 nm as indexed by triangle marks, while at 100 s (G), GISAXS results are consistent with the 2D assemblies of hexagonally packed cylinders with the (11) plane parallel to the membrane surface and with a (10) plane distance of 46 nm as indexed by triangle marks.

in the core) in DOX/THF at the solvent ratios tested above a critical micelle concentration (CMC) of around 0.1−0.5 wt %, *i.e.*, well below the polymer concentrations tested with SAXS. The disorder-to-order boundary, where micelles begin to pack into lattices, was found around 10 wt % polymer. Beyond this boundary, micelles preferentially formed BCC lattices over a polymer concentration range of 10−16 wt %. Above 16 wt % polymer, a Hex lattice emerged for high DOX-fractions above 7:3 DOX/THF, whereas SC lattices were found for lower DOX-fractions.

We hypothesize that the factor differentiating the structural evolution of BCC → Hex from BCC → SC in the phase diagram in Figure 1 is the segregation of the PI-block from the PS-block in the micelle corona. When the DOX-fraction is lower than 7:3 DOX/THF, the PI-block segregates from the PS-block giving rise to additional spherical I-domains at or above 20 wt % polymer. This generates two interpenetrating SC lattices of P4VP and PI micelle cores shifted by half the cubic lattice diagonal, which would present a scattering profile akin to a CsCl simple cubic lattice, consistent with our observation. In contrast, when the DOX solvent fraction is high enough, with DOX, not THF, being the better solvent for the PI-block, PI-block segregation does not take place, and micellar coalescence takes place with increasing concentration, giving rise to a hexagonal lattice of anisotropic, cylinder-like objects.

We next calculated the expected solvent evaporation-induced compositional changes in solution for the ISV/DOX/THF system in the region relevant for the SNIPS membrane formation based on considerations of Raoult's law about the vapor pressures in mixed ideal solutions (see the Supporting Information for detailed calculations, as well as Figure S2).[12] The mobilities of solvents in semidilute polymer solutions may be much slower than those in pure solvents, and therefore the true compositional changes may deviate from such calculations. However, the compositional changes at the relevant region close to the solution−air interface may not deviate substantially from the ideal situation, further motivating this approach.[12] In Figure 2A, the results of such calculations are plotted onto the ternary ISV/DOX/THF phase diagram derived from SAXS measurements shown in Figure 1. Two evaporation trajectories are plotted starting from 10 wt % ISV solutions in 5:5 (trajectory 1 marked with circles) and 3:7 DOX/THF (trajectory 2 marked with triangles) with evaporation time intervals of 10 s. From our calculations, trajectory 1 should cross the BCC−Hex boundary after a 90 s evaporation time, whereas trajectory 2 should cross the BCC−SC boundary after a 70 s evaporation time.

To test the validity of such calculations, *in situ* GISAXS measurements along trajectory 1 were performed. Indeed, results were consistent with a transition from BCC (Figure 2F) to Hex (Figure 2G), corroborating the structural evolution in the ISV/DOX/THF phase diagram. The scattering pattern in Figure 2F taken at a 40 s evaporation of a 10 wt % ISV solution in 5:5 DOX/THF was indexed with a BCC lattice with a 58 nm lattice constant with the ⟨110⟩ direction parallel to the membrane normal direction. The calculated solution composition at this point is 14 wt % ISV concentration in 58:42

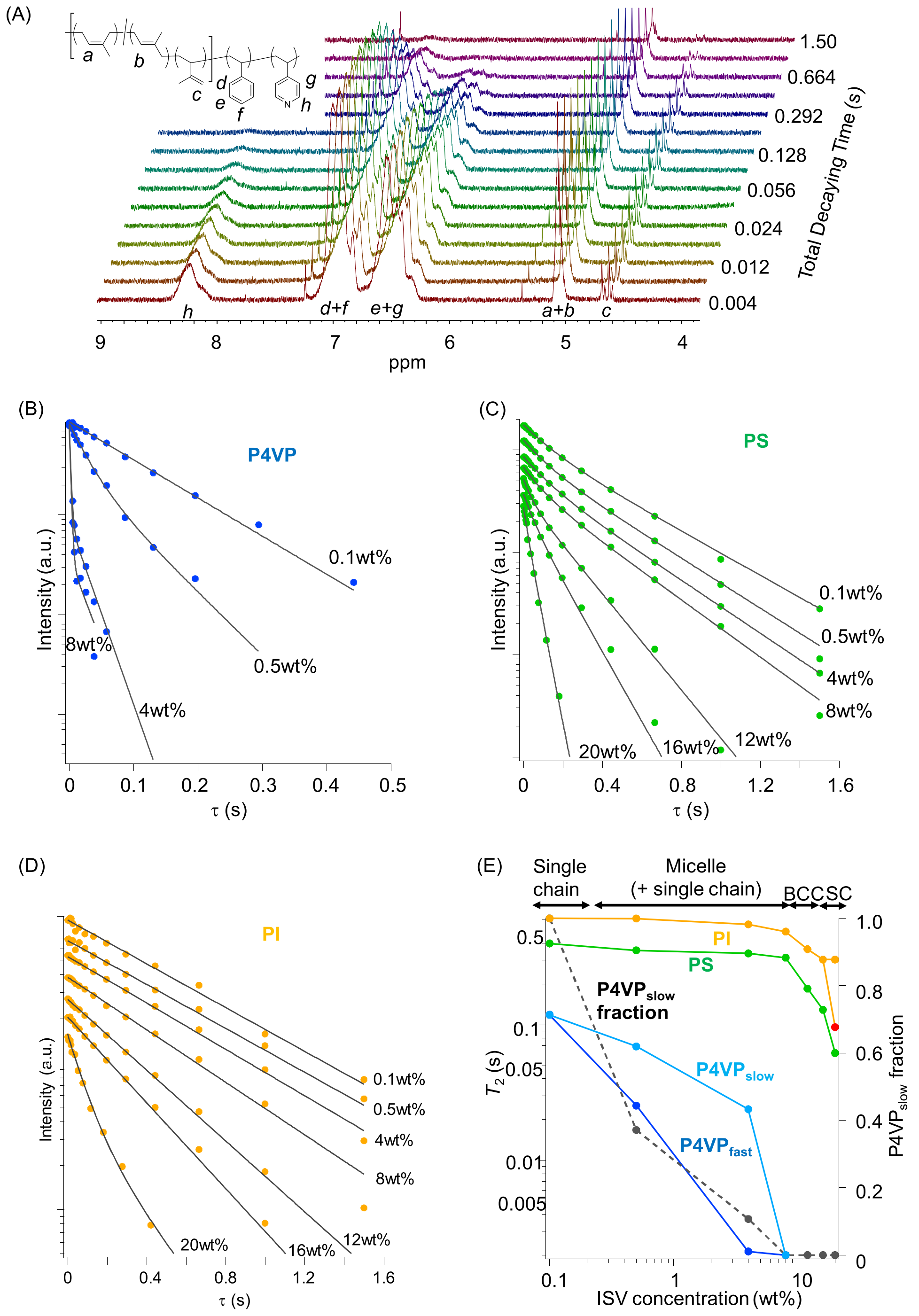

Figure 3. T_2 relaxation analysis for various concentrations of ISV in 4:6 DOX/THF. (A) Representative decay of NMR spectra by T_2 relaxation (0.5 wt %). The following peaks were used for T_2 analysis for individual terpolymer blocks: h for P4VP, d + f for PS, and c for PI. T_2 relaxation behavior for (B) P4VP, (C) PS, and (D) PI-blocks for different ISV concentrations. The *y*-axes show measured signal intensities on a log scale. The intensities were translated along the longitudinal axis to make it easy to view (for a plot of the data without this shift, please see Figure S3 in the Supporting Information). (E) T_2 dependence of each block on ISV concentration: (blue) fast relaxing component of P4VP; (teal) slow relaxing component of P4VP; (green) PS; (orange) slow relaxing component of PI; (red) fast relaxing component of PI; and (black) fraction of slow relaxing component of P4VP.

DOX/THF. The quiescent solution SAXS profiles of 16 and 12 wt % ISVs in 60:40 DOX/THF were thus the closest data points to this *in situ* GISAXS profile in the ternary diagram. The determined BCC lattice constants for these solution SAXS patterns were 61 nm for 16 wt % and 63 nm for 12 wt % (Figure S1D), close to the GISAXS results (58 nm). The scattering pattern in Figure 2G for the same trajectory 1, but moving from a 40 to 100 s evaporation time, was indexed with the 2D assemblies of hexagonally packed cylinders with the (11) plane parallel to the membrane surface and with a (10) plane distance of 46 nm. A solvent evaporation time of 100 s should change the solution composition to 20 wt % ISV in 76:24 DOX/THF, as predicted from our calculations. The quiescent SAXS profile of a 20 wt % ISV solution in 7:3 DOX/

THF with a hexagonal cylinder pattern exhibiting a 47 nm (10) plane distance (Figure S1C) corroborates this *in situ* GISAXS profile. The consistency between these quiescent solution SAXS and *in situ* GISAXS results for trajectory 1, therefore, suggests that Raoult's law regarding the vapor pressures in mixed ideal solutions is a good predictor for the time-dependent concentrations in our experiments.

In addition to quiescent solution and *in situ* scattering experiments, membrane structural evolution was monitored at varying evaporation times before and after crossing the order−order phase boundary by immersing the entire membrane into a water bath and subsequent imaging of the membrane top surface *via* SEM. Interestingly, the surface structures observed in this way along trajectory 1 (Figure 2B−E) were different from what we anticipated from our (quiescent SAXS and *in situ GISAXS*) scattering analysis. The membrane surface quenched at 40 s along the evaporation trajectory 1, which according to scattering results (vide supra) should have formed a BCC lattice with a lattice constant of 58 nm (*in situ* GISAXS) in the precursor solution before quenching, exhibited a square pattern of pores with a pore-to-pore distance of only 40 nm (from fast Fourier transformation (FFT) analysis of the SEM image shown in Figure 2B). Moreover, the membrane surface quenched at 100 s along the same evaporation trajectory 1, which from both quiescent solution SAXS and *in situ* GISAXS results (vide supra) should have formed a hexagonal pattern of cylinders parallel to the surface, also showed a highly ordered square pattern rather than parallel lines (Figure 2C). This inconsistency between SEM imaging results of final membranes and *in situ* GISAXS analysis of casted polymer films during evaporation (as well as quiescent solution SAXS results) suggests that in some cases, the structure at the very top surface of the casted solution gets kinetically trapped or may undergo additional changes upon phase inversion.

In contrast to trajectory 1, quenching experiments along trajectory 2 starting from 10 wt % ISV in 3:7 DOX/THF showed a structural evolution consistent with expectations from the experimental phase diagram in Figure 1. Since for this trajectory, *in situ* GISAXS data was not available, SEM results will be compared to quiescent solution SAXS only. After an evaporation time of 50 s, the predicted solution composition is 16 wt % ISV in 41:59 DOX/THF. The corresponding quiescent solution SAXS profile to this composition exhibited a BCC pattern with a lattice constant of 62 nm (16 wt % ISV in 4:6 DOX/THF; Figure S1F). The resulting membrane surface exhibited hexagonally arrayed pores (see also FFT in the inset of Figure 2D), which is consistent with a projection of a BCC lattice along the ⟨111⟩ direction. The ⟨111⟩ projection of a BCC lattice with a lattice constant of 62 nm provides a hexagonal array with 51 nm pore-to-pore distance (62 nm × $\sqrt{2}/\sqrt{3}$), which is very close to the 50 nm pore-to-pore distance as derived from the FFT analysis of the top surface SEM image in Figure 2D. The membrane surface quenched after an 80 s evaporation time (Figure 2E), *i.e.*, after the anticipated crossing of the BCC−SC order−order transition boundary, exhibited a square array of 45 nm periodicity (FFT analysis of SEM image). The corresponding solution composition was calculated as 20 wt % ISV in 50:50 DOX/THF. The quiescent solution SAXS profile at this composition exhibited an SC scattering pattern with a 44 nm lattice constant (Figure S1E and Table S1), consistent with the SEM results of the membrane top surface.

NMR Investigations of Ternary System ISV/DOX/THF. To further investigate the details of the micellar structure and its packing evolution, in particular, to answer the question of which blocks are in the micelle core and corona, respectively, ^{1}H NMR spin−spin relaxation time (T_2) analysis was conducted at various concentrations from 0.1 to 20 wt % of ISV in 4:6 DOX/THF (see Figures 3 and S3). This series of samples is positioned along the 4:6 DOX/THF isopleth in the ternary ISV/DOX/THF phase diagram in Figure 1B and, with increasing ISV concentration, moves across the disordered → BCC → SC phase transitions. The T_2 analysis for each block was performed based on the following peak assignments marked in Figure 3A: h for P4VP, d + f for PS, and c for PI. We avoided using a + b for PI or e + g for PS and P4VP because of the complexities due to overlapping of more than two nonequivalent protons. The T_2-based signal intensity decays for P4VP, PS, and PI peaks were plotted as a function of decaying time, τ, increasing from 4 ms to 1.5 s with 15 steps (Figure 3B−D). The signal decays were then fitted by mono- or bicomponent exponential functions, as described by the following equations

$$I = I_0\, e^{-\tau/T_2} + I_b \tag{1}$$

$$I = I_{0s}\, e^{-\tau/T_{2s}} + I_{0f}\, e^{-\tau/T_{2f}} + I_b \tag{2}$$

where I is the signal intensity as a function of decay time, τ, I_0 is the signal intensity for $\tau = 0$, and I_b is the baseline noise. Subscripts s and f in eq 2 symbolize slow or fast relaxing components, respectively. The styrene peak intensity for region d + f inherently contains two chemically inequivalent protons, and thus the signal decays associated with this region are always characterized by bicomponent exponentials. Because the T_2 of protons contributing to peak f (one proton in the para ring position) is much shorter (fast relaxing) than that of protons (slow relaxing) contributing to peak d (two protons in the ortho ring position) for a reason, we will discuss later, the following coefficient-fixed bicomponent exponential fitted the region d + f of styrene protons well

$$I = I_0\left(\frac{2}{3}\, e^{-\tau/T_{2s}} + \frac{1}{3}\, e^{-\tau/T_{2f}}\right) + I_b \tag{3}$$

where T_{2s} is the relaxation time of protons in position d, and T_{2f} is that of protons in position f. At the lowest concentration of 0.1 wt % ISV measured, we assume that ISV chains do not form micelles but rather exist as single chains (unimers). As a very crude comparison to rationalize this assumption, the overlap concentration of a 90 kDa PS homopolymer (instead of a 90 kDa 22:51:27 ISV terpolymer) in pure THF (instead of 4:6 DOX/THF) can be estimated from intrinsic viscosity parameters available in the literature (intrinsic viscosity of 41 dL/g, calculated with Mark−Houwink−Sakurada parameters of $K = 0.014$ and $a = 0.70$)[31] and is 2.6 wt %. As shown in Figure 3B, only at this low concentration P4VP showed monoexponential decay behavior as reflected by a straight line in the log-scale plot (see also Figure S3A). Starting at 0.5 wt % and beyond, the decay exhibited bicomponent exponential behavior as reflected by kinks in the respective log plots beyond 0.5 wt %. Furthermore, the T_2 relaxation of P4VP drastically got faster as the concentration increased, as evidenced by the increasing slopes in Figure 3B.

In striking contrast, the T_2 relaxation behavior of PS and PI stayed almost unchanged below 8 wt % (Figures 3C,D and

S3B,C). Changes in the T_2 behavior for all blocks/components are plotted as a function of ISV concentration in Figure 3E. Here, T_2 of the two P4VP components are depicted as blue and teal lines for the fast and slow relaxation components, respectively. These two components of P4VP with very different T_2 at and above 0.5 wt % suggest that there are two distinct environments surrounding ISV. The T_2 relaxation time sensitively reflects molecular motion, especially on the time scale of 0.01−10 s, and molecules undergoing relatively slow motion exhibit shorter T_2 as compared to molecules undergoing fast motion.[32] When the BCP concentration exceeds the critical micelle concentration (CMC), excess amounts of BCP are self-assembled into micelles with core and corona blocks. The core chains segregate out to reduce thermodynamically unfavorable solvent contacts. It is noteworthy that single chains of BCP always coexist with micelles, even beyond the CMC, and that the concentration of such single chains remains fixed beyond the CMC. Because chain motion of core blocks inside micelles should be strongly restricted due to chain entanglements and exclusion of solvents, their magnetization relaxes faster and therefore the T_2 of the block in the micelle core should be much smaller than that of free single chains outside the micelles. It is thus reasonable to assign the component with longer T_2 (slow relaxing) to free single chains and the one with shorter T_2 (fast relaxing) to micelles. Since T_2 relaxation of P4VP drastically got faster as ISV concentration increased and is monoexponential at 0.1 wt % and biexponential at 0.5 wt % and beyond, while PS and PI T_2 relaxation behaviors do not substantially change in this concentration range, we conclude that P4VP is the core-forming block with an ISV CMC between 0.1 and 0.5 wt %. In this picture, both PS- and PI-blocks are located in the micelle corona. This contradicts the prediction of the very first paper on ISV-derived SNIPS membranes that PI is the core-forming block while P4VP is in the corona.[21] At the time, this prediction was not based on measurements but on considerations of the solvent−polymer interaction strength calculated from Hansen solubility parameters (HSPs).[33] Furthermore, simulated HSPs of monomeric units, rather than experimentally determined HSPs of polymers, were used due to the lack of availability of the HSP for polymeric P4VP. It is common for polymers to have higher HSPs than their monomers, which may be the reason for the deviation of the prediction from the current experimental results.[33] From the independence of T_2 from concentration, we conclude that the motion of the corona blocks is as fast as that of these blocks in single chains. The fraction of slow relaxing component of P4VP is represented by the black dashed line in Figure 3E and directly reflects the single-chain fraction. Though single chains always exist, even at high concentrations above 8 wt % ISV, their slow relaxation component becomes hard to detect for very low fractions, as indicated by the black line in Figure 3E above 10 wt %. We also performed water addition experiments to test ISV micelle stability and, in particular, if a micellar flip would take place under water addition as demonstrated for the SV system with the help of SANS experiments (Figure S4).[19] However, 1−3 wt % water additions did not induce substantial differences in T_2 relaxation behavior as compared to the system in the absence of water, suggesting stability against, *e.g.*, micellar flips or dissociation.

From the ternary ISV/DOX/THF phase diagram depicted in Figure 1 based on solution SAXS, for a 4:6 DOX/THF solvent mixture, the disorder-to-order transition occurs around 10 wt %, where disordered micelles start to pack into BCC lattices. Beyond this concentration, most free solvent is absorbed by the polymer, and micelle−micelle corona chain overlap becomes significant, which is expected to restrict the movement of corona blocks and shorten their T_2. Furthermore, between around 16 and 20 wt % ISV, we have hypothesized that further segregation between PI and PS corona blocks leads to micellization driving a BCC to SC order−order transition, which is expected to lead to additional slowing of BCP motions associated with the block driving this additional micellization. From data shown in Figure 3C,D (see also Figure S3B,C) for PS- and PI-blocks, respectively, the T_2 relaxation behavior of both blocks significantly changes between 8 and 12 wt % ISV as reflected by increases in the slopes of their relaxation curves. This is consistent with the interpretation of PS- and PI-blocks in the micelle corona, which in this concentration range is experiencing reduced mobility as a result of the BCC lattice formation, leading to faster T_2 relaxation. Furthermore, between 16 and 20 wt % ISVs, the relaxation behavior for PI switches from mono- to bicomponent exponential behavior (see Figure 3D and the red data point in Figure 3E), consistent with PI-blocks segregating out into PI micelles as part of the BCC to SC transition with the associated substantially reduced mobility further shortening T_2. This T_2 analysis of ISV in 4:6 DOX/THF solutions at varying concentrations is therefore well consistent with the ISV/DOX/THF phase diagram derived from quiescent solution SAXS experiments of the polymer structure and can be summarized as follows:

(i) Below 0.1 wt %, ISV exists as single chains (unimers).
(ii) Between 0.1 and 0.5 wt % ISVs, P4VP segregation induces micellization with P4PV in the core and PS and PI in the corona.
(iii) Around 10 wt % ISV, the absorption of most free solvents by the corona blocks induces micellar BCC lattice formation with P4VP cores and PI/PS coronas.
(iv) Between 16 and 20 wt % ISVs, PI starts to segregate out from PS into spherical domains driving the BCC to SC transition.

NMR Investigations of Ternary System SV/DMF/THF. The insights provided by the T_2 analysis into the structural evolution of ISV in DOX/THF as a function of polymer concentration encouraged us to apply this method to the SV/DMF/THF system, which is the original and most frequently employed system for SNIPS membrane formation. As discussed in prior sections, although the micellar structure for this system has been extensively studied to figure out which blocks form core and corona chains using various approaches, including SAXS, SANS, cryo-SEM/transmission electron microscopy (TEM), and AFM, there still seems to be a lack of consensus. The starting point of the discussion about micellar structure should be the Hansen solubility parameters predicting that THF is the PS-selective solvent, while DMF is the P4VP-selective solvent.[33] However, some studies concluded that P4VP is always the core-forming block even in pure DMF,[17] while others suggested that P4VP is the corona-forming block even in solvent systems with low DMF fraction.[34] One possible explanation for this inconsistency is that the SV micellar structure is very sensitive to experimental parameters, including BCP molar mass, block fractions, THF/DMF ratio, and the amount of water contamination. This is

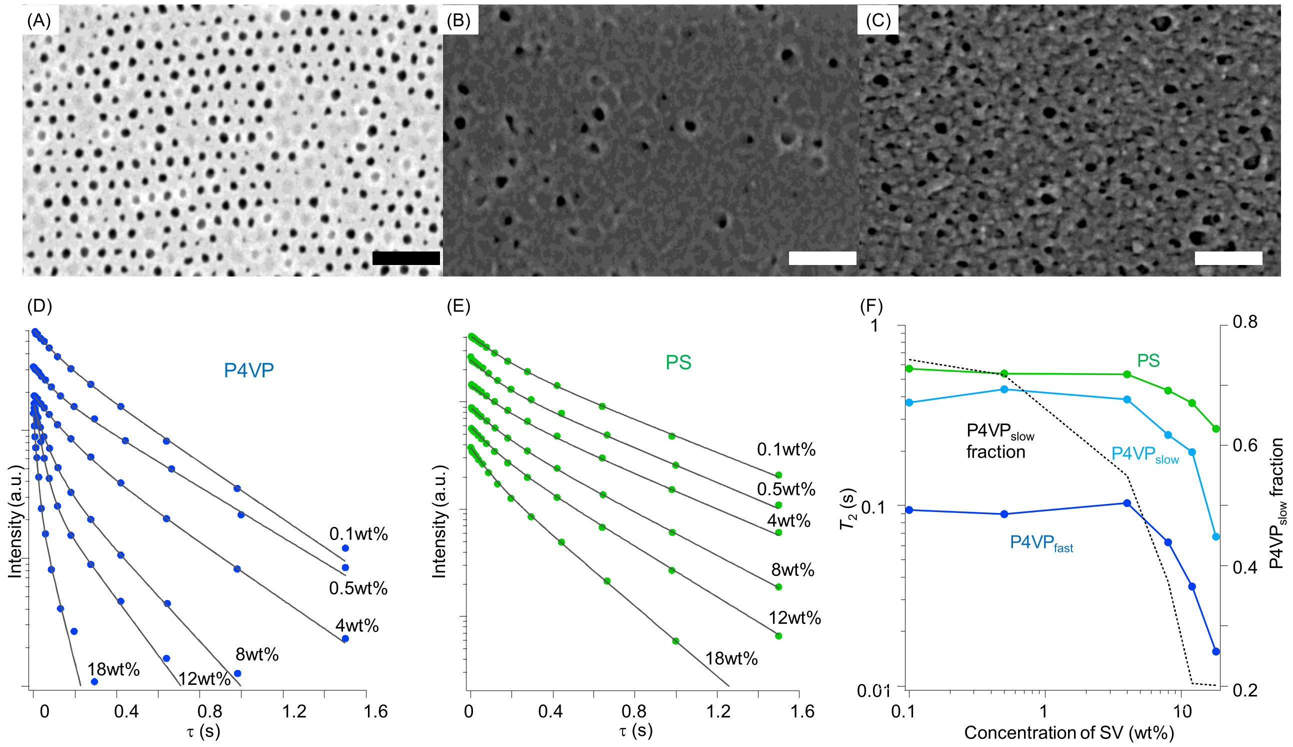

Figure 4. SV micellar structure in the DMF/THF solvent system. (A−C) SEM images of the final membrane top surface structure cast from 18 wt % SV solution in (A) 1:9, (B) 3:7, and (C) 7:3 DMF/THF. T_2 relaxation behavior of (D) P4VP and (E) PS-blocks in 1:9 DMF/THF at various SV concentrations. The *y*-axes show measured signal intensities on a log scale. The intensities were translated along the longitudinal axis to make it easy to view. (F) T_2 dependence of each block on SV concentration: (blue) fast relaxing component of P4VP; (teal) slow relaxing component of P4VP; (green) PS; and (black) fraction of slow relaxing component of P4VP.

consistent with the observation that the SV/DMF/THF system sometimes does not provide periodically ordered top surface layers in the final membranes, although exactly the same solution/casting conditions are employed as reported before.[19] In this context, it is desirable to establish a method to determine details of the micellar structure for a particular BCP system of interest that is generally available, since not every lab may have access to techniques like SANS, SAXS, or cryo-EM so far employed to this end on the SV/DMF/THF system. Solution-state NMR spectroscopy is one of the most ubiquitous characterization techniques for molecular systems, but to the best of our knowledge, it has not been used to determine the micellar structure in the SV/DMF/THF system.

We prepared SV by sequential living anionic polymerization with a molar mass of 95 kDa and a P4VP volume fraction of 0.2 with a dispersity of 1.13. Before we started the investigation of the micellar structure of SV in solution, we tried to figure out suitable casting conditions that provide nicely ordered top surfaces of SNIPS membranes. The resulting surface structures of materials cast from 18 wt % SV solutions with different DMF/THF compositions were characterized by SEM. As shown in Figure 4A−C, in our experiments, only 1:9 DMF/THF solvent mixtures resulted in hexagonally ordered pores, while 3:7 or 7:3 DMF/THF mixtures, which are most frequently used for SV-derived SNIPS membranes, gave disordered top surface structures.[8,34] In particular, we varied the concentration and evaporation time for 7:3 DMF/THF but failed to obtain any ordered surface structures. We thus used the 1:9 DMF/THF solvent system for further investigations of micellar structure.

The T_2 relaxation behaviors for P4VP and PS in SV/DMF/THF solutions in the concentration range of 0.1−18 wt % are shown in Figure 4D,E, respectively (see Figure S5 for the regular proton NMR spectrum of SV/DMF/THF with peak assignments). The distinguishing feature of the T_2 relaxation behavior of P4VP in 1:9 DMF/THF relative to that in the ISV/THF/DOX system is the observation of a bicomponent exponential decay even at 0.1 wt % SV, as evidenced by the nonlinearity in the log-scale plot (Figure 4D). The two components of P4VP in the ISV/DOX/THF system at and beyond 0.5 wt % were assigned to single chain and micellar core behavior of P4VP, but this interpretation seems inappropriate for SV/DMF/THF because it is unlikely that the CMC is lower than 0.1 wt % for SV in this solvent system, which is good for both blocks. Actually, diffusion ordered spectroscopy (DOSY) revealed that the CMC is between 4 and 8 wt %, as we will discuss below. Thus, we cannot conclude that P4VP is the core-forming block just by its biexponential relaxation behavior, and another interpretation is required to account for this observation. The factor differentiating P4VP relaxation behavior of SV/DMF/THF from that of ISV/DOX/THF could be the hydrogen-bond formation between DMF and P4VP. The basicity of the pyridine ring may bind the formyl proton of DMF-bearing weak acidity. This hydrogen-bond formation should be very labile, and thus DMF molecules frequently attach to and detach from pyridine moieties. If this chemical exchange occurs on the millisecond time scale compatible with the pulse intervals in the CPMG sequence, it would accelerate T_2 relaxation due to accelerated dephasing of the transverse magnetization in every echo train.[35−37]

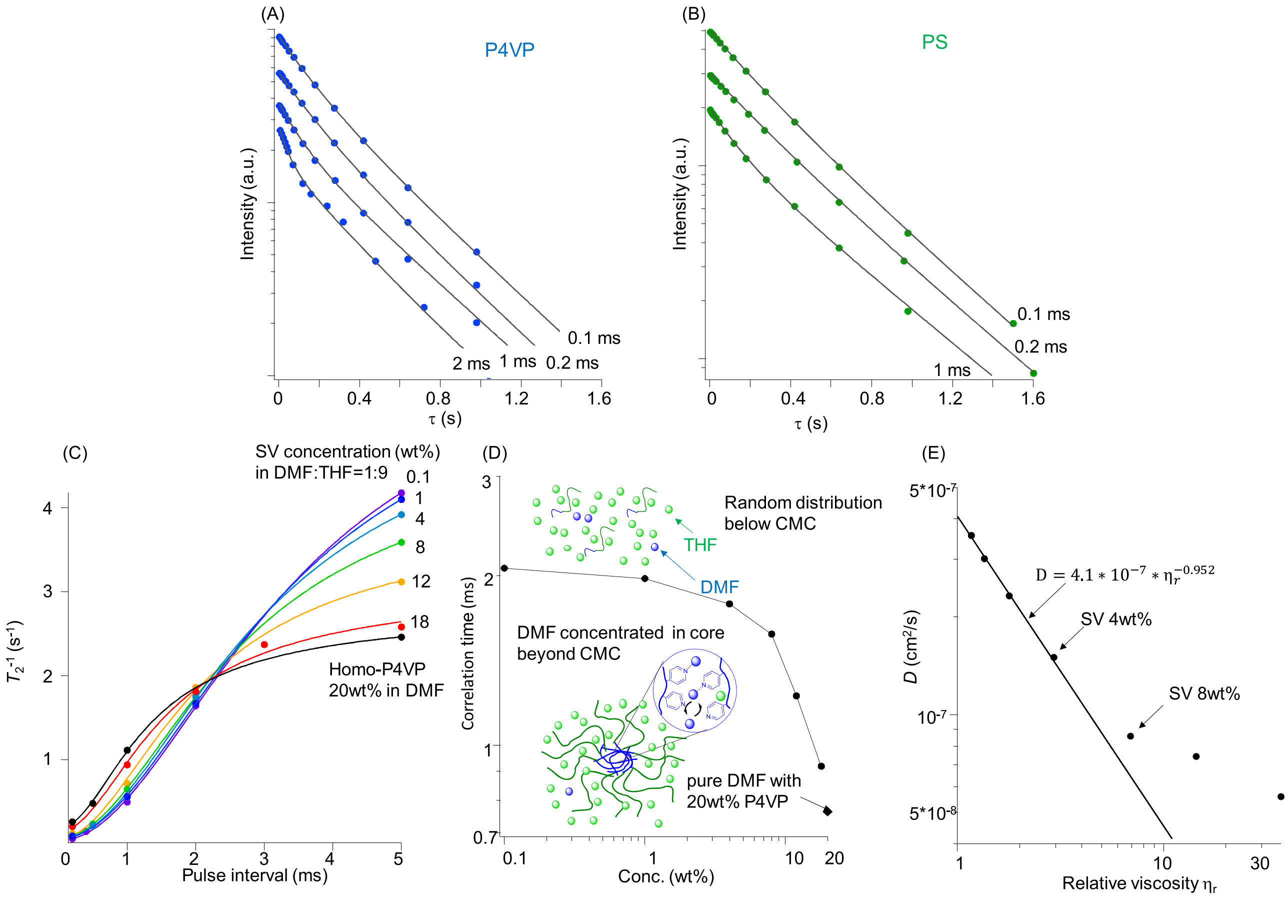

Figure 5. SV micellar structure in 1:9 DMF/THF as revealed by NMR. (A, B) T_2 relaxation dependence of P4VP and PS-blocks on pulse intervals in the CPMG sequence. Fast relaxation components of P4VP and PS are strongly dependent on pulse intervals, while slow relaxation components are independent from it. (C) T_2 relaxation dependence of DMF formyl proton on pulse intervals. SV concentration was changed in the range of 0.1−18 wt %. Black curve is for pure DMF (*i.e.*, without THF) solvating 20 wt % homo-P4VP, which is in the so-called concentrated solution range where polymer chains significantly overlap and entangle. Curve fitting was performed based on eq 4, providing the exchange rate of hydrogen bonding and its correlation time, which is plotted as a function of concentration in (D). (E) Diffusion coefficient determined by DOSY plotted as a function of the relative viscosity calculated by eq 8. The black line was drawn by fitting the first four data points in the low-viscosity region based on eq 7. The slope of the black line was −0.96 (close to −1), showing a good fit to eq 7. The deviation from the line in the high-viscosity region is likely due to micellization, making intrinsic viscosity different from that of single chains. The CMC is thus between 4 and 8 wt % SVs.

To verify this assumption, T_2 of P4VP and PS were measured with various pulse intervals in the CPMG sequence in the range of 0.1−2 ms (Figure 5A). The fast relaxation component of P4VP, which is dominant in the time regime shorter than 0.2 s, strongly depends on the length of the pulse intervals. In contrast, the slow relaxation component dominant in the longer time regime was essentially independent of pulse intervals and stayed constant (see the almost parallel lines in Figure 5A beyond $\tau = 0.2$ s). This relaxation behavior suggests that the fast component of the T_2 relaxation of P4VP stems from reversely catching and releasing DMF molecules *via* hydrogen bonding on the millisecond time scale, while the slow component reflects P4VP chain segments that do not form hydrogen bonds with DMF. The latter may be due to multiple scenarios, including blocking of the active site of pyridine by the major solvent THF, and/or tacticity of the P4VP polymer chains, *e.g.*, mm triads may block DMF approaching the central pyridine unit during the relaxation process (~1 s). Interestingly, the PS relaxation of protons in the para positions of the phenyl ring (fast relaxation) also showed a dependence on the length of the pulse interval, while that of protons in the ortho positions (slow relaxation) did not; see Figure 5B (also see eq 3). The decaying curves in the time regime shorter than 0.3 s got steeper with increasing pulse interval, while those in the time regime beyond 0.3 s stayed constant and thus parallel. This T_2 dependence on the pulse interval of para but not of ortho protons in phenyl rings may suggest that some chemical exchange also takes place in the PS-block. We hypothesize that this is attributable to π−H interactions between the para protons and π-electrons of another phenyl ring, which is a weak interaction with correlation times on the millisecond time scale. Note that this dependence of the PS relaxation on the length of the pulse interval was also observed in the ISV/DOX/THF system, while there was no such dependence for the P4VP relaxation in the non-DMF solvent system.

The effect of pulse intervals on T_2 relaxation, where some chemical exchange takes place, can be expressed by the following equation[35−37]

$$(T_2)^{-1} = \left(\frac{p_A p_B \Delta^2 \omega^2}{k_{ex}}\right)\left\{1 - \frac{\tanh(k_{ex} t_d)}{k_{ex} t_d}\right\} + (T_2{}^0)^{-1} \tag{4}$$

k_{ex} is the exchange rate constant, p_A and p_B are the distribution coefficients between states A and B, t_d is the pulse interval in the CPMG sequence, Δ is the chemical shift difference between the two states, ω is the resonance frequency, and T_2^0 is the relaxation time without chemical exchange. The exchange rate, k_{ex}, can be determined by fitting $(T_2)^{-1}$ *versus* t_d plots with eq 4, providing the correlation time of hydrogen bonding by taking the inverse of k_{ex}. Because the broad P4VP peaks sometimes made it difficult to adjust the phase correctly, we focused on the T_2 dependence on pulse intervals of the DMF formyl proton. The pulse interval was changed in the range of 0.1−5 ms at SV concentrations of 0.1−18 wt % (Figure 5C). The rate of hydrogen-bond exchange is faster with higher pyridine concentration, and thus T_2 of DMF is more susceptible to the pulse interval in the shorter time regime (around 1 ms) for concentrated SV solutions as compared to that for dilute SV solutions. The black curve in Figure 5C is for pure DMF with 20 wt % homo-P4VP as a reference, which is similar to the red curve of an 18 wt % SV solution in 1:9 DMF/THF. The correlation time of forming hydrogen bonds is plotted as a function of SV concentration in Figure 5D. At 0.1 wt % SV, the correlation time is 2 ms and the same as for pure solvents (1:9 DMF/THF) without SV, indicating that DMF forms hydrogen bonds with other DMF molecules and the cross hydrogen bonding with P4VP has minor effects on its relaxation. With increasing SV concentration up to 4 wt %, the correlation time slowly decreases, due to increasing numbers of pyridine units, which promote hydrogen-bond exchange with DMF. Beyond 8 wt %, the correlation time quickly drops down to 0.9 ms at 18 wt % SV, which is a similar time to that observed for a 20 wt % homo-P4VP solution in pure DMF (0.8 ms). Note that SV has only 18 wt % pyridine as compared to homo-P4VP of the same mass, and the solvent used for SV is 1:9 DMF/THF, where the self-exchange of hydrogen bonds between DMF molecules is twice as slow as compared to that of pure DMF (k_{ex} is 440 s^{-1} for 1:9 DMF/THF and 820 s^{-1} for pure DMF). These results suggest that SV in 1:9 DMF/THF generates an environment surrounding DMF molecules similar to that in a concentrated homo-P4VP solution in pure DMF (*i.e.*, without THF). Concentrating pyridine and DMF in the SV/DMF/THF system can be achieved by forming SV micelles with P4VP cores, which are selectively swollen by DMF, as illustrated in the insets of Figure 5D.

The CMC of SV in 1:9 DMF/THF was determined from diffusion coefficients obtained from DOSY NMR experiments. Earlier attempts have been reported to determine the CMC of BCPs by DOSY, but all of them were focused on amphiphilic BCPs in water with very low CMC of less than 0.01 wt %.[38,39] In our case, however, the CMC should be above 4 wt % SV due to good solvent quality, and thus the solution viscosity has to be considered very carefully as a function of polymer concentration. The viscosity, η, of a polymer solution can be expressed as follows

$$\eta = \eta_0\eta_r \tag{5}$$

where η_0 is the solvent viscosity and η_r is the relative viscosity. The Stokes−Einstein equation can then be written as follows[39]

$$D = \frac{K_BT}{6\pi\eta_0R}\frac{1}{\eta_r} \tag{6}$$

$$\log D = \log\frac{K_BT}{6\pi\eta_0R} - \log\eta_r \tag{7}$$

where D is the diffusion coefficient of the polymer, K_B is the Boltzmann constant, and R is the hydrodynamic radius of the polymer. Below the CMC, R is identical to the hydrodynamic radius of a single chain and can be considered as a constant, providing a linear relationship between $\log D$ and $\log \eta_r$. η_r can be expressed as a function of polymer concentration, *e.g.*, using the Huggins equation or Martin equation.[40] These equations are known to deviate from the experimental data in the semidilute regime due to underestimating (Huggins equation) or overestimating (Martin equation) the overlap effect of polymeric components. An equation providing better fitting results in dilute and semidilute regimes is the Martin equation in polynomial form with reduced terms as described below[40]

$$\eta_r = 1 + c[\eta] + K_H(c[\eta])^2 + \frac{K_H{}^2}{2!}(c[\eta])^3 + \frac{K_H{}^3}{3!}(c[\eta])^4 + \frac{K_H{}^4}{4!}(c[\eta])^5 \tag{8}$$

where c is the polymer volume concentration (g/mL), $[\eta]$ is the intrinsic viscosity of SV (37 dL/g: PS value in THF),[31] and K_H is the Huggins constant of 0.24 (PS value in THF).[41] Here, we used PS homopolymer data (instead of 80:20 SV) in pure THF (instead of 1:9 DMF/THF), which is available in the literature. D was then plotted as a function of η_r, showing linear behavior with a slope of −0.96 (close to −1) following eq 7 below 8 wt % (Figure 5E). At 8 wt %, the experimental value starts to deviate from the fit, suggesting micellization changes $[\eta]$ significantly. Thus, these DOSY experiments support a CMC of SV in 1:9 DMF/THF between 4 and 8 wt % SVs. This is consistent with the foregoing T_2 analysis suggesting an environment surrounding SV with DMF drastically changing somewhere between 4 and 8 wt % SVs *via* micellization with a P4VP core swollen with DMF.

■ CONCLUSIONS

In this study, we attempted to better understand micelle formation and the structural evolution of top surface layers of ISV triblock terpolymer-derived ultrafiltration membranes cast from binary DOX/THF solvent mixtures as a function of solvent evaporation. To that end, we combined different methodologies, including structural analysis of quiescent ISV solutions *via* SAXS, calculated solution concentrations and compositions upon solvent evaporation, self-assembly and top surface analysis during solvent evaporation *via in situ* GISAXS, T_2 relaxation analysis of quiescent solutions *via* ^{1}H NMR, and top surface postfabrication analysis *via* SEM. These studies provided a comprehensive picture of the complex structural behavior of this ternary system, starting with (i) micelle formation from terpolymer unimers below 1 wt % ISV, driven by P4VP segregating into micelle cores; (ii) disorder-to-order transitions *via* BCC micelle lattice formation around 10 wt % ISV; and, depending on the DOX/THF solvent composition, (iii) order-to-order transitions from BCC to HEX or BCC to SC lattices, the latter driven by additional segregation of PI from PS corona blocks leading to PI micelles. While in the case of the BCC to HEX transition, details of the structural analysis from quiescent sample studies were not consistent with top surface SEM observations of final membranes, possibly due to kinetically trapped states or structural changes during phase inversion, the overall analysis suggested that equilibrium structure formation considerations are helpful in understanding the observed structural evolution in the top surface layers of such block copolymer self-assembly and nonsolvent-induced phase separation (SNIPS)-based ultrafiltration membranes. We found that, in particular, T_2 relaxation analysis of quiescent polymer solutions in such BCP and binary mixed solvent systems *via* ^{1}H proton NMR spectroscopy is a powerful tool in revealing which blocks are responsible for micelle core and corona chain formations driving the observed structural transitions. Since proton NMR spectroscopy is accessible to a large majority of researchers, we expect this technique to become a particularly powerful tool to understand and predict micelle formation in SNIPS membrane formation processes. As our proton T_2 relaxation analysis of the SV/DMF/THF system demonstrated, however, the correct interpretation of such NMR experiments can be complex, as other dynamical processes (*e.g.*, hydrogen bonding) may mask micelle formation and need to be considered. We found that for the ternary SV/DMF/THF system with 1:9 DMF/THF, P4VP is also the core-forming block with a CMC of around 4−8 wt % SV. Moreover, we concluded that there is a preferential solvent distribution of DMF and THF. Proton relaxation analysis suggested that DMF is highly concentrated in the P4VP micelle core, while THF is mostly excluded from the core and solvates the PS corona chains. Overall, we hope that the understanding of the molecular processes governing structure formation in such complex polymer−solvent systems will ultimately help in designing more advanced SNIPS-derived membranes for applications ranging from clean water to biopharmaceutical separations.

■ ASSOCIATED CONTENT

Supporting Information

The Supporting Information is available free of charge at https://pubs.acs.org/doi/10.1021/acs.macromol.0c00595.

> All solution SAXS profiles used to generate the ternary phase diagram; lattice symmetries and lattice constants from solution SAXS; detailed scattering; and ^{1}H NMR data and their analysis plus calculations of evaporation-induced compositional changes (PDF)

■ AUTHOR INFORMATION

Corresponding Author

Ulrich Wiesner − *Materials Science and Engineering, Cornell University, Ithaca, New York 14853, United States;* orcid.org/0000-0001-6934-3755; Email: ubw1@cornell.edu

Authors

Yusuke Hibi − *Materials Science and Engineering, Cornell University, Ithaca, New York 14853, United States;* orcid.org/0000-0003-4006-1070

Sarah A. Hesse − *Materials Science and Engineering and Chemistry and Chemical Biology, Cornell University, Ithaca, New York 14853, United States*

Fei Yu − *Materials Science and Engineering and Chemistry and Chemical Biology, Cornell University, Ithaca, New York 14853, United States;* orcid.org/0000-0002-8191-8096

R. Paxton Thedford − *Materials Science and Engineering and Robert Frederick Smith School of Chemical and Biomolecular Engineering, Cornell University, Ithaca, New York 14853, United States*

Complete contact information is available at: https://pubs.acs.org/10.1021/acs.macromol.0c00595

Notes

The authors declare no competing financial interest.

■ ACKNOWLEDGMENTS

This work was funded by the National Science Foundation under award DMR-1707836, and R.P.T. was supported by the NSF Graduate Research Fellowship Program under grant number DGE-1650441. The authors acknowledge D. M. Smilgies at the Cornell High Energy Synchrotron Source (CHESS) facility for technical support during the GISAXS experiments. The authors acknowledge I. Keresztes and A. M. Condo at the Cornell's NMR facility for technical support and helpful discussions around NMR data interpretation. The authors also appreciate Aqueous Solutions Aps for providing a free excel file template for making ternary phase diagram published on their website (https://www.phasediagram.dk/template-for-triangular-diagrams-in-ms-excel/). This work is based upon the research conducted at the Center for High Energy X-ray Sciences (CHEXS), which is supported by the National Science Foundation under award DMR-1829070. The SAXS experiments were based upon the research conducted at CHESS, which is supported by the National Science Foundation under award DMR-1332208. This work made use of the Cornell Center for Materials Research Shared Facilities, which are supported through the NSF MRSEC program (DMR-1719875). This work was also supported by JSPS KAKENHI (Grant-in-Aid for JSPS Fellows 1039865 to Y.H.).

■ REFERENCES

(1) Mai, Y.; Eisenberg, A. Self-Assembly of Block Copolymers. *Chem. Soc. Rev.* **2012**, *41*, 5969−5985.

(2) Hoheisel, T. N.; Hur, K.; Wiesner, U. B. Block Copolymer-Nanoparticle Hybrid Self-Assembly. *Prog. Polym. Sci.* **2015**, *40*, 3−32.

(3) Pochan, D. J.; Wooley, K. L.; Cui, H.; Zhong, S.; Chen, Z. Block Copolymer Assembly via Kinetic Control. *Science* **2007**, *317*, 647−650.

(4) Jain, S.; Bates, F. S. Consequences of Nonergodicity in Aqueous Binary PEO-PB Micellar Dispersions. *Macromolecules* **2004**, *37*, 1511−1523.

(5) Tan, K. W.; Wiesner, U. Block Copolymer Self-Assembly Directed Hierarchically Structured Materials from Nonequilibrium Transient Laser Heating. *Macromolecules* **2019**, *52*, 395−409.

(6) Tan, K. W.; Jung, B.; Werner, J. G.; Rhoades, E. R.; Thompson, M. O.; Wiesner, U. Transient Laser Heating Induced Hierarchical Porous Structures from Block Copolymer-Directed Self-Assembly. *Science* **2015**, *349*, 54−58.

(7) Sai, H.; Tan, K. W.; Hur, K.; Asenath-Smith, E.; Hovden, R.; Jiang, Y.; Riccio, M.; Muller, D. A.; Elser, V.; Estroff, L. A.; Gruner, S. M.; Wiesner, U. Hierarchical Porous Polymer Scaffolds from Block Copolymers. *Science* **2013**, *341*, 530−534.

(8) Peinemann, K.; Abetz, V.; Simon, P. F. W. Asymmetric Superstructure Formed in a Block Copolymer via Phase Separation. *Nat. Mater.* **2007**, *6*, 992−996.

(9) Dorin, R. M.; Marques, D. S.; Sai, H.; Vainio, U.; Phillip, W. A.; Peinemann, K. V.; Nunes, S. P.; Wiesner, U. Solution Small-Angle X-ray Scattering as a Screening and Predictive Tool in the Fabrication of Asymmetric Block Copolymer Membranes. *ACS Macro Lett.* **2012**, *1*, 614−617.

(10) Dorin, R. M.; Sai, H.; Wiesner, U. Hierarchically Porous Materials from Block Copolymers. *Chem. Mater.* **2014**, *26*, 339−347.

(11) Pendergast, M. M.; Mika Dorin, R.; Phillip, W. A.; Wiesner, U.; Hoek, E. M. V. Understanding the Structure and Performance of Self-Assembled Triblock Terpolymer Membranes. *J. Membr. Sci.* **2013**, *444*, 461−468.

(12) Stegelmeier, C.; Filiz, V.; Abetz, V.; Perlich, J.; Fery, A.; Ruckdeschel, P.; Rosenfeldt, S.; Förster, S. Topological Paths and Transient Morphologies during Formation of Mesoporous Block Copolymer Membranes. *Macromolecules* **2014**, *47*, 5566−5577.

(13) Gu, Y.; Dorin, R. M.; Tan, K. W.; Smilgies, D. M.; Wiesner, U. In Situ Study of Evaporation-Induced Surface Structure Evolution in Asymmetric Triblock Terpolymer Membranes. *Macromolecules* **2016**, *49*, 4195−4201.

(14) Madhavan, P.; Peinemann, K. V.; Nunes, S. P. Complexation-Tailored Morphology of Asymmetric Block Copolymer Membranes. *ACS Appl. Mater. Interfaces* **2013**, *5*, 7152−7159.

(15) Nunes, S. P.; Behzad, A. R.; Peinemann, K.-V. Self-Assembled Block Copolymer Membranes: From Basic Research to Large-Scale Manufacturing. *J. Mater. Res.* **2013**, *28*, 2661−2665.

(16) Ye, X.; Niroomand, H.; Hu, S.; Khomami, B. Block Copolymer Micelle Formation in a Solvent Good for All the Blocks. *Colloid Polym. Sci.* **2015**, *293*, 2799−2805.

(17) Nunes, S. P.; Sougrat, R.; Hooghan, B.; Anjum, D. H.; Behzad, A. R.; Zhao, L.; Pradeep, N.; Pinnau, I.; Vainio, U.; Peinemann, K. V. Ultraporous Films with Uniform Nanochannels by Block Copolymer Micelles Assembly. *Macromolecules* **2010**, *43*, 8079−8085.

(18) Nunes, S. P.; Behzad, A. R.; Hooghan, B.; Sougrat, R.; Karunakaran, M.; Pradeep, N.; Vainio, U.; Peinemann, K. V. Switchable PH-Responsive Polymeric Membranes Prepared via Block Copolymer Micelle Assembly. *ACS Nano* **2011**, *5*, 3516−3522.

(19) Oss-Ronen, L.; Schmidt, J.; Abetz, V.; Radulescu, A.; Cohen, Y.; Talmon, Y. Characterization of Block Copolymer Self-Assembly: From Solution to Nanoporous Membranes. *Macromolecules* **2012**, *45*, 9631−9642.

(20) Marques, D. S.; Dorin, R. M.; Wiesner, U.; Smilgies, D. M.; Behzad, A. R.; Vainio, U.; Peinemann, K. V.; Nunes, S. P. Time-Resolved GISAXS and Cryo-Microscopy Characterization of Block Copolymer Membrane Formation. *Polymer* **2014**, *55*, 1327−1332.

(21) Phillip, W. A.; Mika Dorin, R.; Werner, J.; Hoek, E. M. V.; Wiesner, U.; Elimelech, M. Tuning Structure and Properties of Graded Triblock Terpolymer-Based Mesoporous and Hybrid Films. *Nano Lett.* **2011**, *11*, 2892−2900.

(22) Pendergast, M. T. M.; Mika Dorin, R.; Phillip, W. A.; Wiesner, U.; Hoek, E. M. V. Understanding the Structure and Performance of Self-Assembled Triblock Terpolymer Membranes. *J. Membr. Sci.* **2013**, *444*, 461−468.

(23) Li, Y. M.; Srinivasan, D.; Vaidya, P.; Gu, Y.; Wiesner, U. Asymmetric Membranes from Two Chemically Distinct Triblock Terpolymers Blended during Standard Membrane Fabrication. *Macromol. Rapid Commun.* **2016**, *37*, 1689−1693.

(24) Dorin, R. M.; Phillip, W. A.; Sai, H.; Werner, J.; Elimelech, M.; Wiesner, U. Designing Block Copolymer Architectures for Targeted Membrane Performance. *Polymer* **2014**, *55*, 347−353.

(25) Ilavsky, J.; Jemian, P. R. Irena: Tool Suite for Modeling and Analysis of Small-Angle Scattering. *J. Appl. Crystallogr.* **2009**, *42*, 347−353.

(26) Ilavsky, J. Nika: Software for Two-Dimensional Data Reduction. *J. Appl. Crystallogr.* **2012**, *45*, 324−328.

(27) Busch, P.; Rauscher, M.; Smilgies, D. M.; Posselt, D.; Papadakis, C. M. Grazing-Incidence Small-Angle X-Ray Scattering from Thin Polymer Films with Lamellar Structures - The Scattering Cross Section in the Distorted-Wave Born Approximation. *J. Appl. Crystallogr.* **2006**, *39*, 433−442.

(28) Smilgies, D. M.; Blasini, D. R. Indexation Scheme for Oriented Molecular Thin Films Studied with Grazing-Incidence Reciprocal-Space Mapping. *J. Appl. Crystallogr.* **2007**, *40*, 716−718.

(29) Smilgies, D. M.; Li, R.; Giri, G.; Chou, K. W.; Diao, Y.; Bao, Z.; Amassian, A. Look Fast: Crystallization of Conjugated Molecules during Solution Shearing Probed in-Situ and in Real Time by X-ray Scattering. *Phys. Status Solidi RRL* **2013**, *7*, 177−179.

(30) Carr, H. Y.; Purcell, E. M. Effects of Diffusion on Free Precession in Nuclear Magnetic Resonance Experiments. *Phys. Rev.* **1954**, *94*, 630−638.

(31) Mandema, W.; Zeldenrust, H. Diffusion of Polystyrene in Tetrahydrofuran. *Polymer* **1977**, *18*, 835−839.

(32) Kimmich, R.; Fatkullin, N. Polymer Chain Dynamics and NMR. *Adv. Polym. Sci.* **2004**, *170*, 1−113.

(33) Hansen, C. M. *Hansen Solubility Parameters: A User's Handbook*, 2nd ed.; CRC Press: New York, 2007.

(34) Marques, D. S.; Vainio, U.; Chaparro, N. M.; Calo, V. M.; Bezahd, A. R.; Pitera, J. W.; Peinemann, K. V.; Nunes, S. P. Self-Assembly in Casting Solutions of Block Copolymer Membranes. *Soft Matter* **2013**, *9*, 5557−5564.

(35) Spěváček, J.; Hanyková, L. NMR Study on Polymer-Solvent Interactions during Temperature-Induced Phase Separation in Aqueous Polymer Solutions. *Macromol. Symp.* **2007**, *251*, 72−80.

(36) Spěváček, J.; Starovoytova, L.; Hanyková, L.; Kouřilová, H. Polymer-Solvent Interactions in Solutions of Thermoresponsive Polymers Studied by NMR and IR Spectroscopy. *Macromol. Symp.* **2008**, *273*, 17−24.

(37) Larsson, G.; Martinez, G.; Schleucher, J.; Wijmenga, S. S. Detection of Nano-Second Internal Motion and Determination of Overall Tumbling Times Independent of the Time Scale of Internal Motion in Proteins from NMR Relaxation Data. *J. Biomol. NMR* **2003**, *27*, 291−312.

(38) Bakkour, Y.; Darcos, V.; Li, S.; Coudane, J. Diffusion Ordered Spectroscopy (DOSY) as a Powerful Tool for Amphiphilic Block Copolymer Characterization and for Critical Micelle Concentration (CMC) Determination. *Polym. Chem.* **2012**, *3*, 2006−2010.

(39) Groves, P. Diffusion Ordered Spectroscopy (DOSY) as Applied to Polymers. *Polym. Chem.* **2017**, *8*, 6700−6708.

(40) Matsuoka, S.; Cowman, M. K. Equation of State for Polymer Solution. *Polymer* **2002**, *43*, 3447−3453.

(41) Spychal, T.; Lath, D.; Berek, D. Thermodynamic and Hydrodynamic Properties of the the Systems Polymer-Tetrahydrofuran-Water: 1. Solution Properties of Polystyrene. *Polymer* **1979**, *20*, 437−442.